

## Effects of strain and defects on the topological properties of $\text{HfTe}_5$

Na Hyun Jo,<sup>1,2,\*</sup> Omar A. Ashour<sup>3,4,5,\*</sup> Zhixue Shu,<sup>6</sup> Chris Jozwiak<sup>1</sup>, Aaron Bostwick<sup>1</sup>, Yang Wang,<sup>2</sup> Eoghan Downey,<sup>2</sup> Sae Hee Ryu<sup>1</sup>, Kai Sun,<sup>2</sup> Tai Kong,<sup>6</sup> Sinéad M. Griffin,<sup>4,5,‡</sup> and Eli Rotenberg<sup>1,§</sup>

<sup>1</sup>*Advanced Light Source, Lawrence Berkeley National Laboratory, Berkeley, California 94720, USA*


<sup>2</sup>*Department of Physics, University of Michigan, Ann Arbor, Michigan 48109, USA*

<sup>3</sup>*Department of Physics, University of California, Berkeley, California 94720, USA*

<sup>4</sup>*Materials Science Division, Lawrence Berkeley National Laboratory, Berkeley, California 94720, USA*

<sup>5</sup>*Molecular Foundry, Lawrence Berkeley National Laboratory, Berkeley, California 94720, USA*

<sup>6</sup>*Department of Physics, University of Arizona, Tucson, Arizona 85721, USA*

 (Received 23 February 2024; revised 19 April 2024; accepted 17 May 2024; published 10 June 2024)

Manipulating topological states is a topic of vigorous research. However, the impact of such topological phase transitions on the quasiparticle dynamics remains elusive. In this work, we present the effects of a transition from a strong to weak topological insulator in  $\text{HfTe}_5$  as a function of Te vacancy concentration. We observed a significant transition from distinct sharp surface states and Dirac crossing to a Fermi-liquid-like quasiparticle state in which these surface-localized features are heavily suppressed. Additionally, by inducing the same effect through applied uniaxial stress, we demonstrate that changes in the lattice constants play the foremost role in determining the electronic structure, self-energy, and topological states of  $\text{HfTe}_5$ . Our results demonstrate the possibility of using both defect chemistry and strain as control parameters for topological phase transitions and associated many-body physics.

DOI: [10.1103/PhysRevB.109.235122](https://doi.org/10.1103/PhysRevB.109.235122)

### I. INTRODUCTION

Unlike traditional phase transitions, which are described by symmetry breaking and the onset of an order parameter, quantum spin Hall (QSH) phases arise only for electronic states of particular topologies. The change in the electronic topology between a bulk material and the vacuum gives rise to protected surface states. Ever since topological insulators were realized in three-dimensional bulk materials, tuning their associated QSH edge states has been of great interest. Although such gapless surface states are robust with respect to various perturbations, time-reversal-symmetry (TRS) breaking through Coulomb and magnetic perturbations is known to open a gap, for example, in the presence of randomly distributed Fe atoms [1]. Recent studies further imply that exotic states, such as axion insulators, can arise in the presence of ordered magnetic atoms with certain crystalline symmetries [2–6]. While controlling topological states with the spin degree of freedom has been thoroughly explored, other degrees of freedom, including lattice, charge, and orbital orders, are less prevalent in the literature.

After the discovery of topological materials in the 2010s,  $\text{HfTe}_5$  and  $\text{ZrTe}_5$  gained attention due to the range in their reported, and often conflicting, topological properties. Experimentally,  $\text{HfTe}_5$  and  $\text{ZrTe}_5$  were variously reported to

be Dirac semimetals, weak topological insulators (WTIs), or strong topological insulators (STIs) [7–19]. Discrepancies exist between reports not only for the reported topological properties but also regarding temperature-dependent band changes [12,14–16,20] and novel magnetotransport properties [21–23]. These discrepancies have been attributed to either different sample defects or different measurement conditions. Recent studies tend to support the idea that sample defects, particularly Te vacancies, can significantly influence the transport properties [24,25]. However, there is still a lack of systematic studies examining the electronic structure changes as a function of defects. Additionally, vacancy defects not only alter the local bonding environment but also impact the local bond lengths. It remains unclear which of these factors has a more pronounced effect on the electronic structure and, consequently, on the observed topological phase of these systems.

Considering the most recent hydrostatic pressure and uniaxial strain studies on  $\text{ZrTe}_5$  [26–28], which demonstrate tuning the topological phases with strain and pressure, the lattice must also have a significant effect on these materials. Diverging claims from first-principles calculations have revealed the sensitivity of the electronic and topological properties to the structural parameters, choice of exchange-correlation functional, and often-neglected finite-temperature effects [29,30]. Nonetheless, these works all highlight the extreme sensitivity of  $\text{HfTe}_5$  and  $\text{ZrTe}_5$  to external perturbations, placing them near critical points for electronic and topological phase transitions. In fact  $\text{ZrTe}_5$  has been suggested as a low-mass dark matter detection target owing to its proximity to this critical point, motivating the accurate characterization

\*These authors contributed equally to this work.

†Contact author: [nhjo@umich.edu](mailto:nhjo@umich.edu)

‡Contact author: [sgriffin@lbl.gov](mailto:sgriffin@lbl.gov)

§Contact author: [erotenberg@lbl.gov](mailto:erotenberg@lbl.gov)

and control of its topological and electronic properties [29]. As a result, the existing experimental studies on the electronic structure of  $\text{ZrTe}_5$  have primarily focused on the opening and closing of the band gap through applied strain at the Fermi energy to show the critical point. However, there is a lack of understanding regarding the influence of such topological phase transition on the self-energy of both surface and bulk electronic states.

In this work, we successfully synthesized single crystals of  $\text{HfTe}_5$  with different vacancy densities. We studied the impact of Te vacancy concentration using a combination of electronic transport and angle-resolved photoemission spectroscopy (ARPES). Dramatic transformations in the band structure, including the appearance and disappearance of surface-localized states meeting at a Dirac crossing, were observed with an increasing number of vacancies. Crucially, we were able to reverse such changes in the band structure with applied uniaxial stress characterized by a liquidlike quasiparticle spectral function. We present density functional theory (DFT) calculations incorporating either different strains or Te vacancies, demonstrating similar bandstructure transformations with lattice constant, and supporting the existence of a topological phase transition in  $\text{HfTe}_5$  with either strain or Te vacancies. In fact, we are not aware of any ARPES study, on any materials system, in which there is direct control of the electronic self-energy with uniaxial stress. The importance of this finding, confirmed through its demonstrated reversibility, extends well beyond topological materials to quantum materials in general.

## II. EXPERIMENTAL AND THEORETICAL METHOD

### A. Crystal growth

Single crystals of  $\text{HfTe}_5$  were grown using tellurium flux. Hafnium powder (Alfa Aesar, 99.6% metals basis excluding Zr, Zr nominal 2–3.5%) and a tellurium lump (Alfa Aesar, 99.999%), in the atomic ratio of Hf:Te = 1:99, were sealed in a silica tube under vacuum. The growth was heated up to 650°C in 3 h, dwell for 10 h, and then slowly cooled to 460°C over 78 h before decanting. Low temperature annealing was conducted at 380°C and 250°C for 5 days in a sealed silica tube for sample 1 and sample 2, respectively. The samples crystallize in space group number 63 ( $Cmcm$ ). The lattice parameters for the single crystals are  $a \sim 3.97 \text{ \AA}^{-1}$ ,  $b \sim 14.5 \text{ \AA}^{-1}$ , and  $c \sim 13.7 \text{ \AA}^{-1}$ .

### B. Electrical transport measurements

Resistance measurements down to 1.8 K were conducted using a Quantum Design physical property measurement system (PPMS) Dynacool using the resistivity option. To have good electrical contacts, the samples were manually masked into a six-probe Hall bar geometry with current direction along the  $a$  axis, and Au films were evaporated to form ohmic contacts. 25- $\mu\text{m}$ -diameter Pt wires were attached to the samples using DuPont silver paint (4929N) in standard four-probe configurations. Magnetic field (0–90 kOe) was applied perpendicular to  $a$  axis.

### C. ARPES measurements

ARPES experiments were conducted at the Beamline 7.0.2 (MAESTRO) at the Advanced Light Source. The data were acquired using the micro-ARPES endstation, which consists of an Omicron Scienta R4000 electron analyzer. Samples were cleaved *in situ* by carefully knocking off an alumina post that is attached on top of each sample with silver epoxy. Data were collected with photon energies of 101 eV, which accesses near the  $\Gamma$  plane of the Brillouin Zone (BZ). The beam size was  $\sim 15 \mu\text{m} \times 15 \mu\text{m}$ . ARPES measurements were performed at  $T = 200 \text{ K}$  under ultra-high vacuum (UHV) better than  $4 \times 10^{-11}$  torr.

As shown in Fig. 2(a),  $\text{HfTe}_5$  has a weak van der Waals bonding along the crystallographic  $b$  direction; thus, the cleaved surface was  $ac$  plane. Note that, by ARPES convention,  $k_z$  is normal to the cleaved surface. Therefore, we define  $x$ ,  $y$ , and  $z$  as directed along the crystallographic  $a$ ,  $c$ , and  $b$ , respectively.

### D. Uniaxial stress

ARPES measurements under uniaxial stress were carried out using a custom-built uniaxial stress cell, as shown in Fig. 6. Samples were mounted with Stycast epoxy (2850FT). After curing the epoxy, we put silver paste (Dupont, 4929N) on top to ground the sample. The uniaxial stress was applied on samples along the crystallographic  $a$  direction. In this experimental configuration, three strain tensor components were nonzero in Voigt notation [31]. We measured the strain tensor component  $\epsilon_{xx}$  with a strain gauge (Fig. 7), and the maximum tensile and compress strain was  $\sim \pm 0.7\%$ . Detailed information about the cell can be found in SI. To keep the same beam spot on the sample, we used a microscope in the  $\mu$ -ARPES chamber. In addition, we performed  $xy$  scan on the sample with 10  $\mu\text{m}$  step size and slit-deflector scan each and every time we change the strain on the sample. Note that we obtained the unstrained data after cooling down the cell but before applying any voltages on the piezo actuators. Even though no voltages are applied, the thermal contraction of the cell, which is most likely different from the thermal contraction of the sample, does slightly exist.

### E. DFT calculations

Our DFT calculations were performed using the Vienna *Ab initio* Simulation Package (VASP) [32–35] using the projector augmented wave (PAW) method [36]. All calculations in the main text use the primitive cell, except those for Fig. 2(d) which used a  $2 \times 2 \times 2$  supercell of 96 atoms. Hf(5p, 6s, 5d) and Te(5s, 5p) electrons were treated as valence. We expanded the wavefunction plane waves to an energy cutoff of 600 eV, and used  $\Gamma$ -centered k-point grids of  $10 \times 8 \times 6$  for the conventional cell,  $12 \times 12 \times 6$  for the primitive cell for structural optimizations, and  $4 \times 4 \times 2$  for the supercell defect structural optimizations. An  $18 \times 14 \times 10$  grid was used with the conventional cell for accurate electronic structure calculations and to generate the Wannier-based tight-binding model. We did not include spin-orbit coupling in our structural optimizations as it was found to have minimal influence on the calculated lattice parameters; however, we included spin-orbit

coupling self-consistently in the electronic structure calculations where specified. The electronic convergence criterion is set to  $10^{-7}$  eV and the force convergence criterion is set to  $0.005$  eV/Å.

Prior DFT calculations on ZrTe<sub>5</sub> and HfTe<sub>5</sub> highlighted the importance of accurate calculations of the structural parameters, particularly owing to the extreme sensitivity of details of the electronic and topological properties on the volume and structure [29]. Therefore, we carefully chose our exchange-correlation functional by benchmarking against reported low-temperature x-ray diffraction measurements, finding PBEsol to give good agreement with the experiment. We calculated the lattice parameters to be  $a = 3.953$  Å,  $b = 14.564$  Å, and  $c = 13.622$  Å using PBEsol, compared to the values measured via powder diffraction at 10 K ( $a = 3.964$  Å,  $b = 14.443$  Å, and  $c = 13.684$  Å) [37].

For the slab calculations, an 11-layer (132-atom) centrosymmetric slab with 15 Å of vacuum was utilized. We used a  $\Gamma$ -centered  $6 \times 20 \times 1$   $k$ -grid, and spin-orbit coupling was included self-consistently. Line thickness and color scale in the slab band structures [Figs. 5(b)–5(f)] are given by Eq. (1):

$$W_{nk} = \sum_{\tau_{\perp}} \sum_{\tau_{\parallel}} \sum_{lm} |\langle \beta_{lm}(\boldsymbol{\tau}) | \psi_{nk} \rangle|^2 e^{-\alpha \tau_{\perp}}, \quad (1)$$

where  $|\psi_{nk}\rangle$  is the Bloch function of band  $n$  at  $k$ -point  $\mathbf{k}$ .  $|\beta_{lm}(\boldsymbol{\tau})\rangle$  is a localized atomic state with orbital quantum numbers ( $lm$ ), centered at an atom with coordinates  $\boldsymbol{\tau} = (\tau_{\parallel}, \tau_{\perp})$ , where  $\tau_{\perp}$  is the nonperiodic direction of the slab. For a given band  $n$  and  $k$ -point  $\mathbf{k}$  in the band structure, we first sum over all quantum numbers ( $lm$ ) of atomic states  $|\beta_{lm}\rangle$ , from all atoms with coordinates  $\boldsymbol{\tau}_{\parallel}$  on a given plane  $\tau_{\perp}$ . We finally sum over all the planes with various  $\tau_{\perp}$ , with an exponential weighting factor  $e^{-\alpha \tau_{\perp}}$  that decays away from the surface of the slab at  $\tau_{\perp} = 0$ . The last sum is performed over the top half of the centrosymmetric slab, giving the weighted projections from one of the surfaces at  $(n, \mathbf{k})$ . Here, we used  $\alpha = 1/5$  Å<sup>-1</sup>.

Using our first-principles electronic structure, we constructed our Wannier function-based tight-binding models using the WANNIER90 package [38], including the Hf- $d$  and Te- $p$  orbitals as basis. Besides the explicit DFT slab calculations mentioned above, we further calculated the surface states by generating a semi-infinite slab configuration from our tight-binding model using the iterative Green's function (IGF) method to generate surface Te-projected bands using the WannierTools [39] package. Finally, our topological invariants were calculated using symmetry indicators and DFT-calculated eigenvalues as implemented in the SYMTOPO [40] package, IRREP [41,42] package and the CHECK TOPOLOGICAL MAT. tool on the Bilbao Crystallographic Server [43].

Gaps (I) and (II) were checked across the entire irreducible Brillouin zone (IBZ) at all levels of strain to ensure the bands do not touch (i.e., the gap remains open) using a  $k$ -grid of  $36 \times 36 \times 12$ . In all cases but one, the minimum gap size was on the order of 10 meV. However, the bands got closer than 10 meV in the case of gap (II) at equilibrium, so it was further checked with a dense cubic “patch” centered around the  $k$ -point with the gap minimum. This calculation showed that the bands almost touch within 1 meV, which is beyond

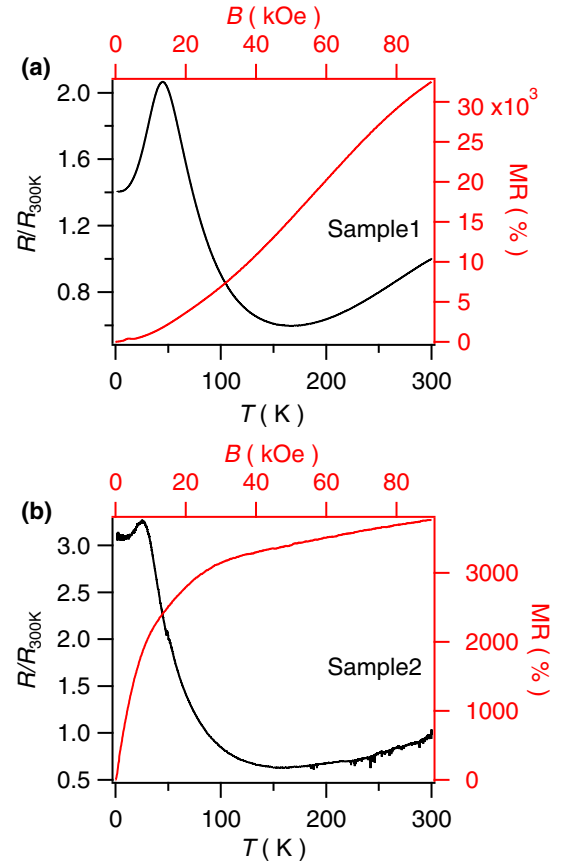


FIG. 1. Electrical transport. (a) Temperature-dependent resistance ratio (left and bottom axis) and MR (right and top axis) of HfTe<sub>5</sub> sample 1 that is post-annealed at 380°C. (b) Temperature-dependent resistance ratio (left and bottom axis) and MR (right and top axis) of HfTe<sub>5</sub> sample 2 that is post-annealed at 250°C.

the resolution of DFT. Thus, gap (II) practically closes at this level of strain at the DFT level. However, since gap (II) is finite for both compressive and tensile strain, we expect any small deviation from the equilibrium structure calculated in DFT to result in gap (II) opening.

### III. RESULTS AND ANALYSIS

We grew single crystals of HfTe<sub>5</sub> with different concentrations of Te-vacancies [25] by adjusting annealing temperatures after the growth (details can be found in Methods). Electrical transport measurements were performed to characterize those samples. As shown in Fig. 1, the temperature of maximum relative resistance,  $T_{\max}$ , for sample 1 is higher ( $\sim 50$  K) than that of sample 2 ( $\sim 20$  K). Additionally, magnetoresistance ( $\text{MR} = 100 \times [R(H) - R(0)]/R(0)$ ) behaviors are very different: first, sample 1 has almost one order higher MR value at 90 kOe compared to the MR of sample 2. Second, MR saturates around 20 kOe for sample 2, while it does not saturate until 90 kOe for sample 1.

We first consider the influence of Te vacancies on our structural and electronic properties via DFT calculations for HfTe<sub>5</sub> in the  $Cmcm$  structure. The conventional unit cell consists of four Hf-Te zigzag chains along the unit cell  $a$  direction,

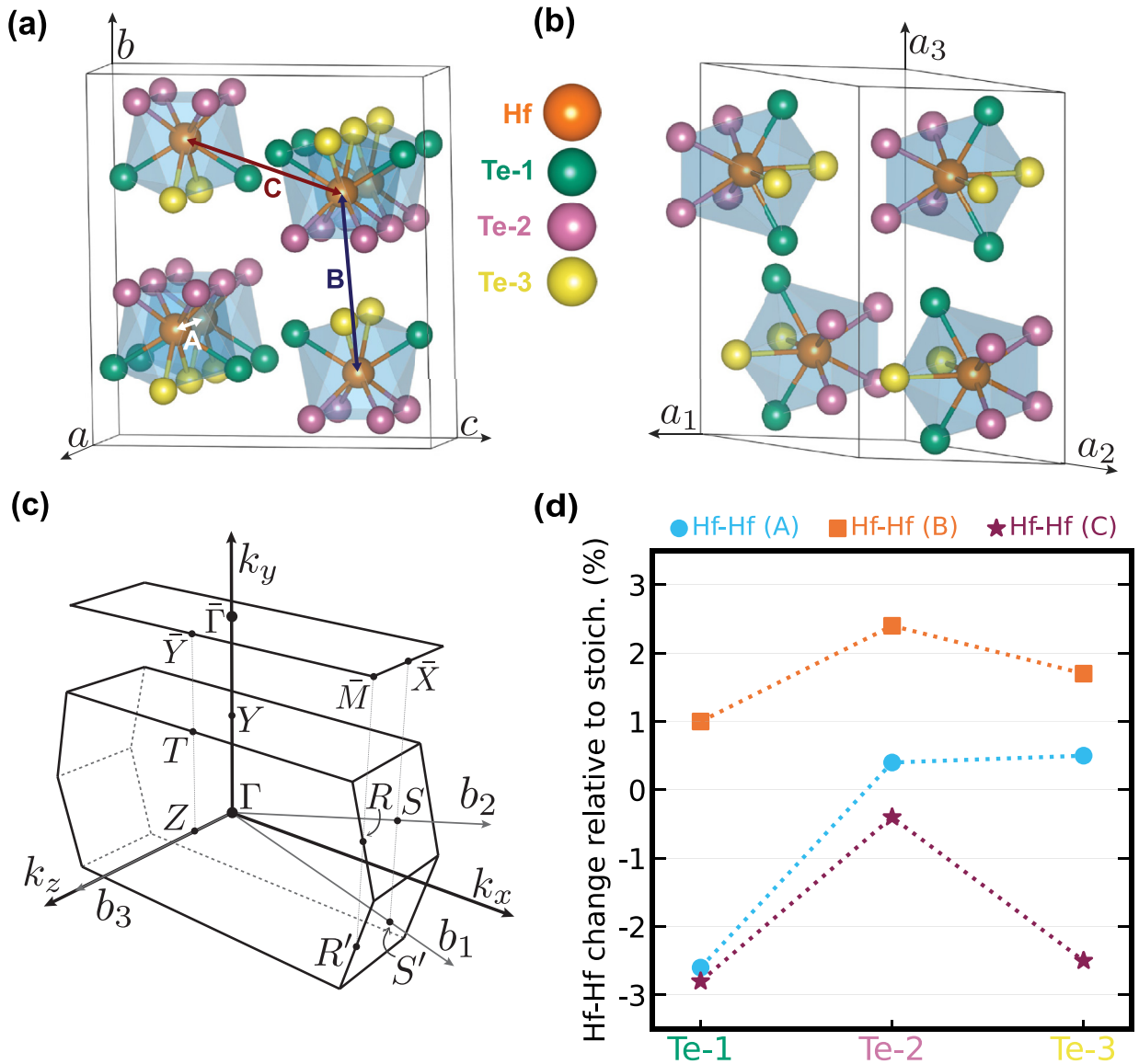


FIG. 2. (a) Conventional cell of  $\text{HfTe}_5$ , depicting the three unique Te sites and Hf-Hf bonds. (b) Primitive cell of  $\text{HfTe}_5$ . The primitive cell has half the volume and number of atoms of the conventional cell, and was used for all bulk DFT calculations. (c) Brillouin zone (BZ) of the primitive cell, along with the BZ of the  $(1\bar{1}0)$  surface.  $b_i$  are the reciprocal lattice basis vectors of the bulk BZ, corresponding to  $a_i$  in panel (b). (d) Structural changes with Te vacancies. Calculated structural changes for  $\text{HfTe}_5$  with the inclusion of Te vacancies on the three unique Te sites in the  $Cmcm$  structure.

as indicated in Fig. 2(a). Within each chain, the atoms are strongly bonded, while the chain-chain bonding is of a weak van der Waals type. There are three unique Te sites (Te-1, Te-2, Te-3). Each Hf atom is bonded to two singly coordinated Te-1 atoms perpendicular to the chains, while Te-2 and Te-3 are doubly coordinated to Hf and participate in the zigzag chain structures. We define three relevant Hf-Hf distances: A (intrachain separation), and B, C [interchain separations roughly along conventional unit cell axes  $b$ ,  $c$ , respectively, see Fig. 2(a)].

The results of our full structural optimizations with vacancies are summarized in Fig. 2(d). We find that Te-2 is the lowest energy defect site; in comparison, Te-1 and Te-3 have energies 2.29 and 8.54 meV higher per atom, respectively. Te-1 vacancies reduce the A intrachain separation and C in-

terchain separation by about 3%, while the Te-2 vacancy has minimal effect on those two distances. Both vacancies lead to a slight increase in the Hf-Hf B interchain separation. Since both vacancies are overall quite close in energy, and much more favorable than the Te-3 vacancy, we can conclude that defects induce a compression along  $a$ , accompanied by a slight increase in the Hf-Hf B interchain separation and another reduction in the Hf-Hf C interchain separation. Considering the association of Te vacancies with compaction of the Hf-Hf interchain distance A, we hypothesize that compressive uniaxial strain along the crystallographic  $a$  direction is a proxy for Te vacancies, or conversely, tensile uniaxial stress along  $a$  may suppress the effects of Te vacancies.

We conducted ARPES measurements on the samples, which have varying vacancy densities, following the electrical

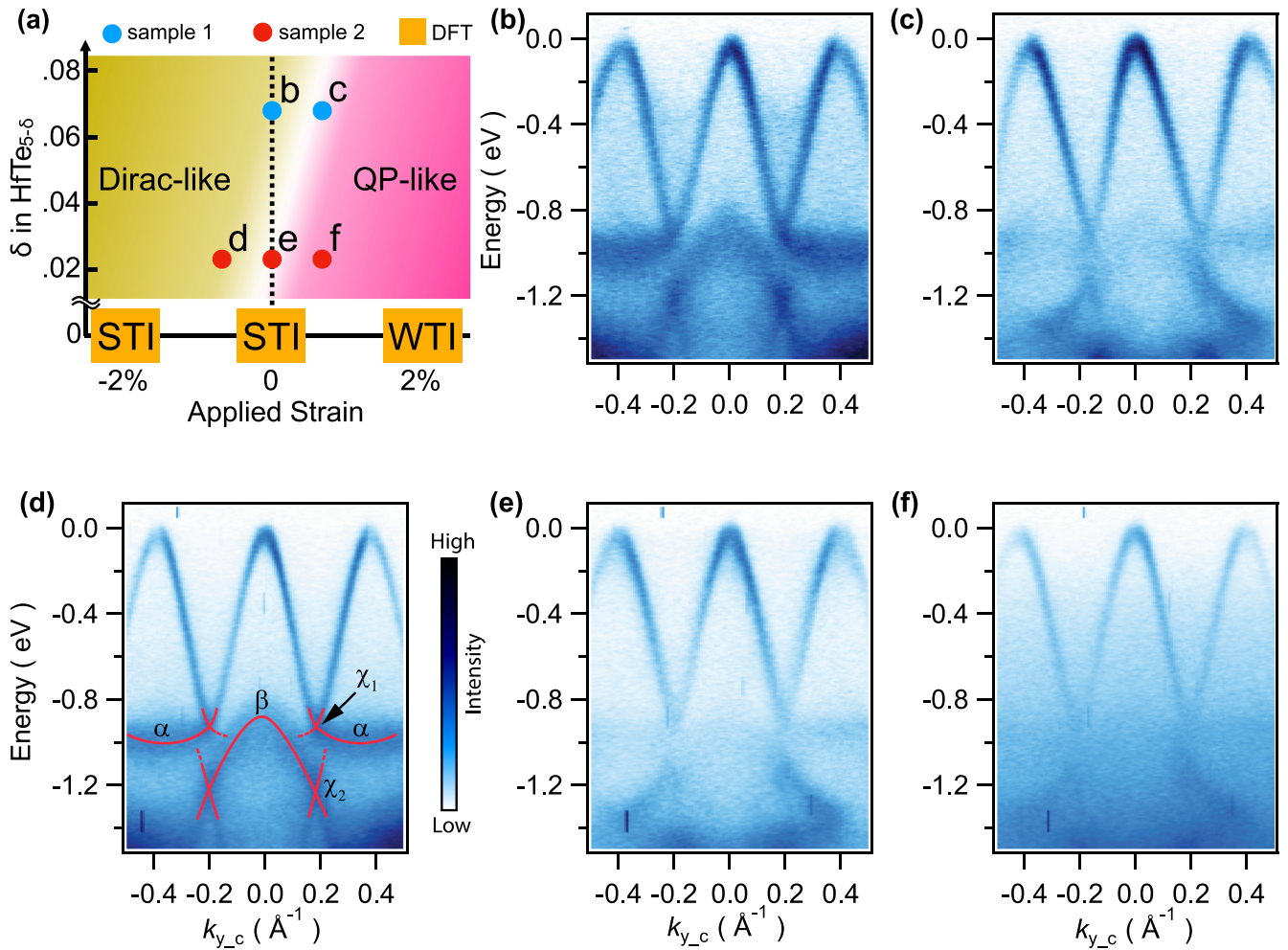


FIG. 3. Topological phase diagram and electronic band structure along  $k_y$  with different Te vacancies and strain. (a) Schematic phase diagram, indicating the location of ARPES band structure measurements in the space of defect density vs strain. Blue markers correspond to Sample 1 and panels (b), (c); red markers correspond to Sample 2 and panels (d)–(f). (b)–(f) ARPES band structures acquired for positions indicated in panel (a).

transport experiments. Additionally, we carried out strain-dependent ARPES experiments on both samples as indicated by the DFT calculation. Figures 3(b)–3(f) are band structure cuts along the high symmetry line  $k_x = 0$ , which corresponds to the  $c$  axis or  $k_y$  direction perpendicular to the Hf chains. Each band structure map corresponds to a different defect density and strain, as summarized schematically in Fig. 3(a) for sample 1 (more defects, blue symbols) and sample 2 (fewer defects, red symbols).

We first discuss the effect of defect density for unstrained samples [Figs. 3(b) and 3(e)]. Although there is little observed difference between the band structures near the Fermi energy, clear differences can be observed near binding energy  $E_B \sim 1$  eV. Interestingly, two Dirac-like band crossings labeled  $\chi_i$  ( $i = 1, 2$ ), appear at  $k_y = \pm 0.2 \text{ \AA}^{-1}$  and  $E_B \sim 0.95$  eV and 1.2 eV in Fig. 3(b). These linear crossings [labeled in Fig. 3(d) where they also appear] are connected, respectively, by relatively flat bands  $\alpha$  and a hole band  $\beta$ . It should be noted that, while in a repeated zone scheme  $\alpha$  and  $\beta$  bands are present in every BZ, matrix element effects modulate the strength of these bands such that  $\alpha$  is suppressed in the central zone and  $\beta$  is suppressed in the second (outer) BZs.

A primary finding of this work is that the features  $\alpha$ ,  $\beta$ , and  $\chi_i$  in Fig. 3(b) vanish when defect density is reduced, Fig. 3(e). These results demonstrate that these features are strongly enhanced by defects in unstrained samples, a counterintuitive result since one usually expects defects to weaken, not enhance, spectral weight. Close inspection of Fig. 3(e) reveals some weak remnant intensity of the  $\alpha$ ,  $\beta$  bands, but the crossings  $\chi_2$  are replaced by some states around  $-1.3$  eV with clearly different dispersion.

Now we discuss the application of uniaxial stress along the  $a$  direction, i.e., in the Hf-Hf chain direction. The resulting strains are estimated to be in the range  $\sim \pm 0.7\%$  based on strain gauge measurements with the same experimental configuration [see Figs. 7 and 12(a)]. For a high defect density combined with tensile strain [sample 1, Fig. 3(c)], the  $\alpha$ ,  $\beta$ , and  $\chi_i$  bands are greatly diminished, similar to unstrained sample 2 [Fig. 3(e)]. In fact, the spectral functions in Figs. 3(c) and 3(e) are practically indistinguishable, the main difference being that the spectra from the sample with more defects (1) has a higher diffuse background. However, applying compressive strain to sample 2 results in the reappearance of the  $\alpha$ ,  $\beta$ , and  $\chi_i$  bands [Fig. 3(d)], with spectral function

very similar to Fig. 3(b). Furthermore, in the case of tensile strain, the surface bands are completely extinguished and there is a notable rise in the diffuse background [Fig. 3(f)], which increases systematically towards higher binding energies. The changes in Figs. 3(d) and 3(f) are fully reversible (see Fig. 12). These changes indicate that with compressive strain, the quasiparticle scattering rate dramatically diminishes, while with tensile strain, there is a large enhancement of the quasiparticle scattering rate, suggestive of enhanced Fermi liquid-type excitations.

From these observations we can conclude the following: (1) The similarity of Figs. 3(b) and 3(d) and of Figs. 3(c) and 3(e) confirms our hypothesis that defects play a similar role as compressive strain along the chain with respect to promoting the appearance of the states  $\alpha$ ,  $\beta$ , and  $\chi_i$ ; (2) these bands appear in  $\text{HfTe}_{5-\delta}$  as a consequence of the lattice changes induced by defects and are not derived from local electronic states directly associated with the defects; (3) defects and tensile strain independently increase the scattering rate, while compression reduces it; (4) up to the maximum applied strain  $\pm 0.7\%$  we do not increase the number of defects; this follows from the reversibility of the changes in Figs. 3(d)–3(f) and 12; (5) if we consider the presence of states  $\alpha$ ,  $\beta$ , and  $\chi_i$  as an indicator of the phase transition, then it occurs within the range of 0–0.2% compressive strain, as shown in Fig. 12.

We first consider the influence of Te vacancies on our structural and electronic properties via DFT calculations for  $\text{HfTe}_5$  in the  $Cmcm$  structure. The conventional unit cell consists of four Hf-Te zigzag chains along the unit cell  $a$  direction, as indicated in Fig. 2(a). Within each chain, the atoms are strongly bonded, while the chain-chain bonding is of a weak van der Waals type. There are three unique Te sites (Te-1, Te-2, Te-3). Each Hf atom is bonded to two singly coordinated Te-1 atoms perpendicular to the chains, while Te-2 and Te-3 are doubly coordinated to Hf and participate in the zigzag chain structures. We define three relevant Hf-Hf distances:  $A$  (intrachain separation), and  $B, C$  [interchain separations roughly along conventional unit cell axes  $b, c$ , respectively; see Fig. 2(a)].

The results of our full structural optimizations with vacancies are summarized in Fig. 2(d). We find that Te-2 is the lowest energy defect site; in comparison, Te-1 and Te-3 have energies 2.29 and 8.54 meV higher per atom, respectively. Te-1 vacancies reduce the  $A$  intrachain separation and  $C$  interchain separation by about 3%, while the Te-2 vacancy has minimal effect on those two distances. Both vacancies lead to a slight increase in the Hf-Hf  $B$  interchain separation. Since both vacancies are overall quite close in energy, and much more favorable than the Te-3 vacancy, we can conclude that defects induce a compression along  $a$ , accompanied by a slight increase in the Hf-Hf  $B$  interchain separation and another reduction in the Hf-Hf  $C$  interchain separation.

To better understand the experimental findings, we carried out DFT calculations under applied strain. To be specific, we simulate strain along the  $a$  axis (i.e., along the Hf-Hf chain direction). We artificially fixed the  $a$  lattice parameter, and found the corresponding optimal lattice parameters for  $b$  and  $c$  for each value of strain considered (2% uniaxial compressive and tensile strain). For all cases, full internal coordinate optimizations were performed. Note that the strain value utilized

TABLE I. The  $\mathbb{Z}_2 = (\nu_0; \nu_1\nu_2\nu_3)$  topological invariants and classification of gaps (I) and (II) at three different levels of strain.  $\nu_0$  is the strong invariant, and  $\nu_{i=1,2,3}$  are the three weak invariants [44,45]. The weak invariants quoted here are with respect to the primitive reciprocal lattice vectors defined in Fig. 2(b).

Gap	2% Compressive		Equilibrium		2% Tensile	
	$\mathbb{Z}_2$	Class	$\mathbb{Z}_2$	Class	$\mathbb{Z}_2$	Class
I	(1;110)	Strong	(1;110)	Strong	(0;110)	Weak
II	(0;110)	Weak	(0;110)	Weak	(0;110)	Weak

in our experiment is approximately one-third of the theoretical calculation. The DFT calculations underestimate the  $a$  lattice parameter by  $\sim 0.43\%$  compared to the values measured in our samples (see Methods). The strain values used in the calculations were selected because, at the DFT level and with the lattice constant underestimation in mind, the STI to WTI transition happens at higher strains, between 1.5% and 1.75% tensile strain, as shown in Table II and discussed in the Appendices.

The bulk primitive electronic structures at the three different levels of strain are shown in Figs. 4(a), 4(b), and 4(c). We find two topological gaps of interest, labeled (I) and (II), whose  $\mathbb{Z}_2$  topological invariants are summarized in Table I. Gap (I) is a strong gap in the  $-2\%$  (compressive) and 0% (equilibrium) strain cases, and a weak gap in the case of  $+2\%$  (tensile) strain. Gap (II) is a weak gap at all strain levels. We conclude that in the absence of defects,  $\text{HfTe}_5$  undergoes a STI  $\rightarrow$  WTI topological phase transition between 0 and 2% tensile strain. Note that the 2% compressive strain case cannot be rigorously labeled a strong topological *insulator* since the bulk system is metallic, as shown in Fig. 4(a). However, the band structure in Fig. 4(a) can be adiabatically deformed so that no bands cross the Fermi level. Thus,  $\text{HfTe}_5$ , under 2% compressive strain is equivalent to a strong topological insulator from the perspective of band topology. We expect that  $\text{HfTe}_5$  remains an insulator when smaller compressive strains are applied.

A topological surface state at the  $\bar{\Gamma}$  point at the Fermi energy is shown in Figs. 5(b), 5(d) and 5(e). This state lies in gap (I), which is a strong topological gap at equilibrium and with compressive strain, so we expect an odd number

TABLE II. The bulk  $\mathbb{Z}_2$  topological invariant and associated topological classification calculated at various levels of strain.

Strain	$a$ (Å)	$\mathbb{Z}_2$	Class
-2.00%	3.874	(1;110)	STI
-1.50%	3.894	(1;110)	STI
-1.00%	3.913	(1;110)	STI
-0.50%	3.933	(1;110)	STI
0.00%	3.953	(1;110)	STI
+0.50%	3.973	(1;110)	STI
+1.00%	3.993	(1;110)	STI
+1.50%	4.012	(1;110)	STI
+1.75%	4.022	(0;110)	WTI
+2.00%	4.032	(0;110)	WTI

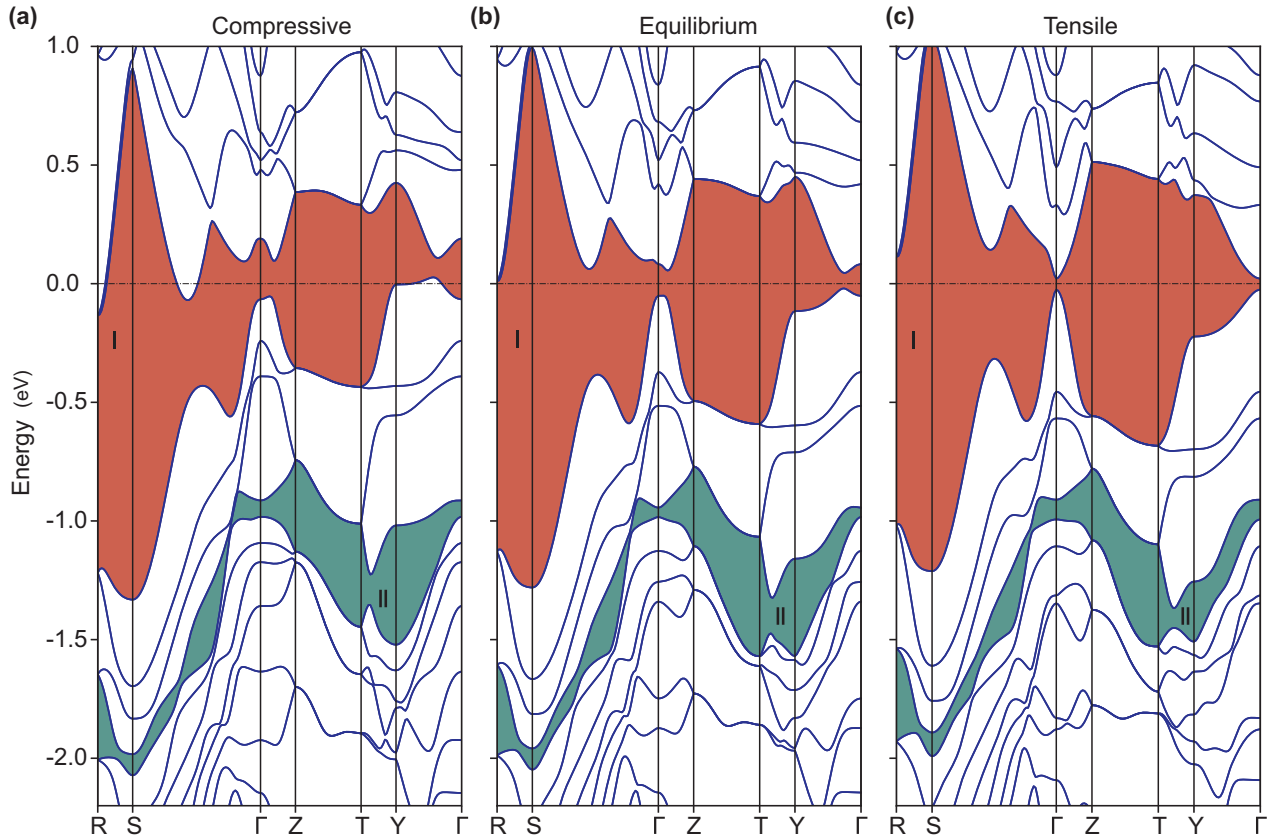


FIG. 4. Effect of Te vacancies and strain on the crystal structure and electronic structure of HfTe<sub>5</sub> (a)–(c) Calculated electronic band structures of HfTe<sub>5</sub> under uniaxial compressive strain, at equilibrium, and under uniaxial tensile strain, as defined in the main text. The two topological gaps of interest are shaded and labeled as (I) and (II). The Fermi level in each is set to 0 eV and marked by a dashed line.

of topological surface states [44,45] (namely, one topological state at equilibrium in this system). With tensile strain, gap (I) becomes weak and the topological surface state at  $\bar{\Gamma}$  is gapped out [Figs. 5(c) and 5(f)]. No topological surface states are present on the  $(1\bar{1}0)$  surface in gap (I) with tensile strain, however. If we identify the surface with the  $\mathbf{G} = (1, -1, 0)$  reciprocal lattice vector, then we have  $\mathbf{G} \bmod 2 = G_v$ , where  $G_v = (v_1, v_2, v_3) = (1, 1, 0)$ . Thus, in the weak TI state, the  $(1\bar{1}0)$  surface cannot host any topological surface states [44,45] in gap (I).

Figure 5(a) shows a band structure cut along the  $k_y = 0$ , which corresponds to the  $\bar{\Gamma} - \bar{X}$  direction. The topological surface state at the Fermi energy is not clearly resolved from the bulk states, similar to previous ARPES studies for ZrTe<sub>5</sub> and HfTe<sub>5</sub> [12,16,18], but overall band structures are amazingly well matched with the DFT calculations.

#### IV. DISCUSSION

The phase diagram in Fig. 3(a) summarizes the observed phases. The upper left region (more defects and/or compressive strain) has a Dirac-like spectrum characterized by the appearance of the  $\alpha$  and  $\beta$  bands connecting linear crossings  $\chi_i$  around  $E_B \sim 1.1$  eV. The lower right region (fewer defects and/or tensile strain) is characterized by the absence of these states. Furthermore, there is a strong correlation between tensile strain applied along the  $a$  axis and the quasiparticle

scattering rate. The latter represents a transition towards a liquidlike quasiparticle (QP) phase, characterized by spectral weight transfer from the bands to a strong diffuse background that increases systematically with binding energy.

To understand these features around  $E_B \sim 1.1$  eV, we next compare our ARPES results to the DFT results. As previously mentioned, we note that the strain considered in the DFT calculations is about three times the strain on the sample in the experimental measurements, thus the changes are more pronounced between the compressive strain, equilibrium, and tensile strain band structures. However, the equilibrium DFT calculation results [Fig. 5(e)] reproduce the essential features of unstrained sample 1 [Fig. 3(b)] and compressed sample 2 [Fig. 3(d)], namely the shapes and relative locations of bands  $\alpha$ ,  $\beta$  and crossings  $\chi_{1,2}$ . Since the calculation does not include photoemission matrix element effects, the bands appear equally in all BZs.

From these surface electronic structure calculations, we next interrogate the surface projected bands for the presence of topologically protected states. Although both  $\chi_{1,2}$  are suggestive of Dirac crossings, neither of them are predicted by DFT to be a topological surface state. Since gap (II) is a weak gap, we expect an even number of topological surface states [44,45]. However, since we have  $\mathbf{G}_v = (v_1, v_2, v_3) = (1, 1, 0)$ , similar to gap (I), no topologically nontrivial surface states can be expected on the  $(1\bar{1}0)$  surface of HfTe<sub>5</sub> in gap (I) for the same reason previously discussed.

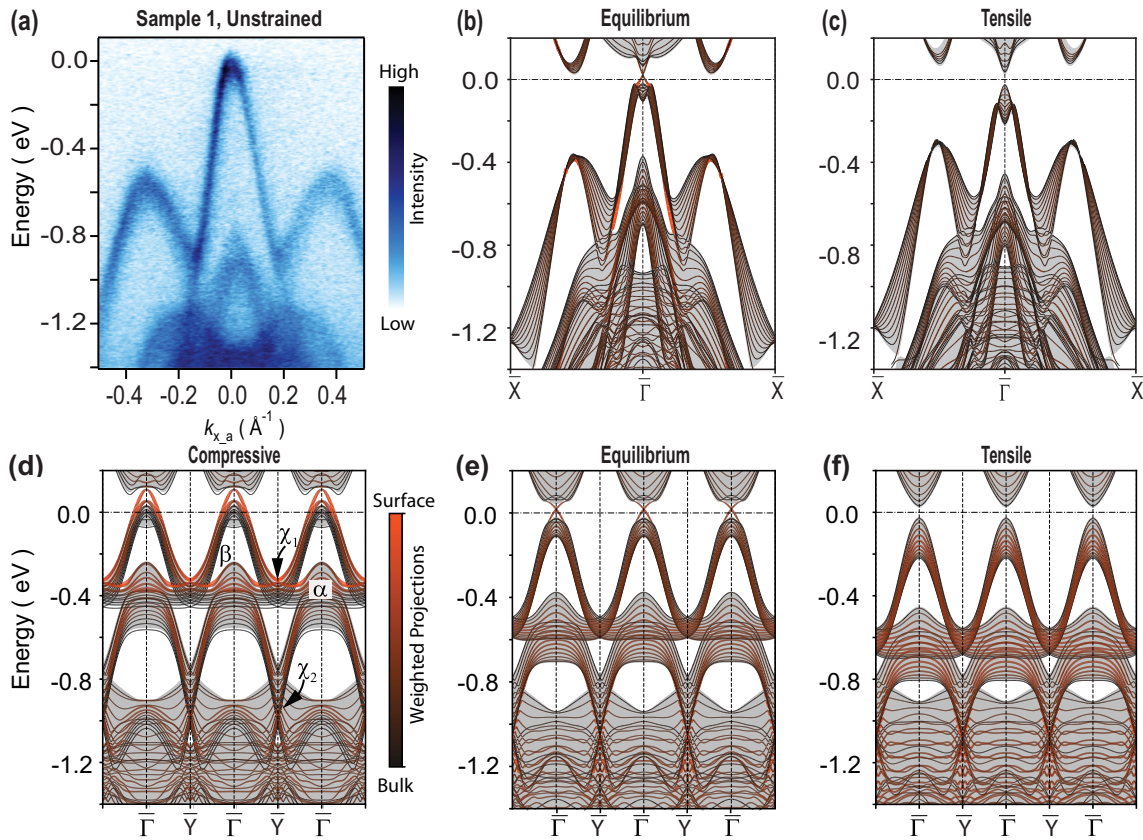


FIG. 5. Nontrivial topological states at  $\bar{\Gamma}$ . (a) Electronic band structure along the  $k_x$  of sample 1 at ambient condition. (b), (c) Slab band structures along the  $\bar{\Gamma} - \bar{X}$  direction for equilibrium, and tensile strain, respectively. (d), (f) Calculated surface band structure along the  $\bar{\Gamma} - \bar{Y}$  direction of pristine  $\text{HfTe}_5$  with compressive strain, at equilibrium, and with tensile strain, respectively. The gray shading represents bulk bands projected onto the  $(1\bar{1}0)$  surface, while the colored lines represent the slab bands. The color and line width of the slab bands are given by Eq. (1) in the supplementary information, with thin black lines representing bulk character and thick red lines representing surface character.

Considering the  $\alpha, \beta$  and crossings  $\chi_{1,2}$  bands are not directly related to the TI surface states, the enhancement of the spectral weight of the bands with more defects is counterintuitive. Thus, it leads us to connect with the topological phase transition near the Fermi energy. For TI surface states at or near the Fermi energy, the interplay between topology and disorder effects has been well studied [45]: surface states of a strong or weak TI are robust or vulnerable against charge disorders and thus the surface is expected to be conductive and insulating. In contrast, at energy far away from the Fermi en-

ergy (e.g., in the gap between two valence bands), impurities also have some nontrivial impact on surface states, through a different mechanism: broadening of line width due to disorder potentials. In contrast to a homogeneous electric potential, which shifts the energy of all bands by a constant amount, random potentials created by charge impurities provide random shifts, which results in a broadening of the line width. For the surface of a strong TI, the conducting topological surface state screens the Coulomb potential from charge impurities, reducing the disorder potential and thus leading to a sharper spectrum. This effect applies equally to surface states both near and away from the Fermi energy. In contrast, for weak TIs, such screening effects are absent, and thus the spectrum becomes more diffusive. As a result, if a material undergoes a topological phase transition from a strong TI to a weak TI, this effect implies that surface states away from the Fermi energy shall suffer more from impurity potential in the weak TI phase. This surface screening effect will logically affect the surface states most strongly. This is largely consistent with what was observed in the ARPES measurement, where the surface states ( $\alpha, \beta$  and crossings  $\chi_{1,2}$ ) become diffusive in the weak TI phase, while bulk states at the same energy range remain largely unchanged.

What remains to be explained is the reversible correlation between the topological class and the notable changes to the diffuse scattering background, which reflect

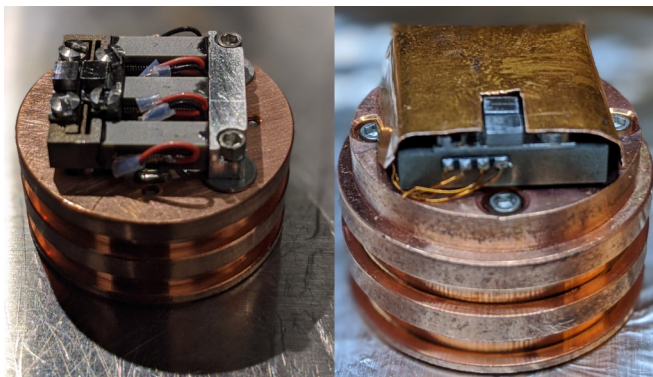


FIG. 6. Uniaxial stress cell for ARPES.



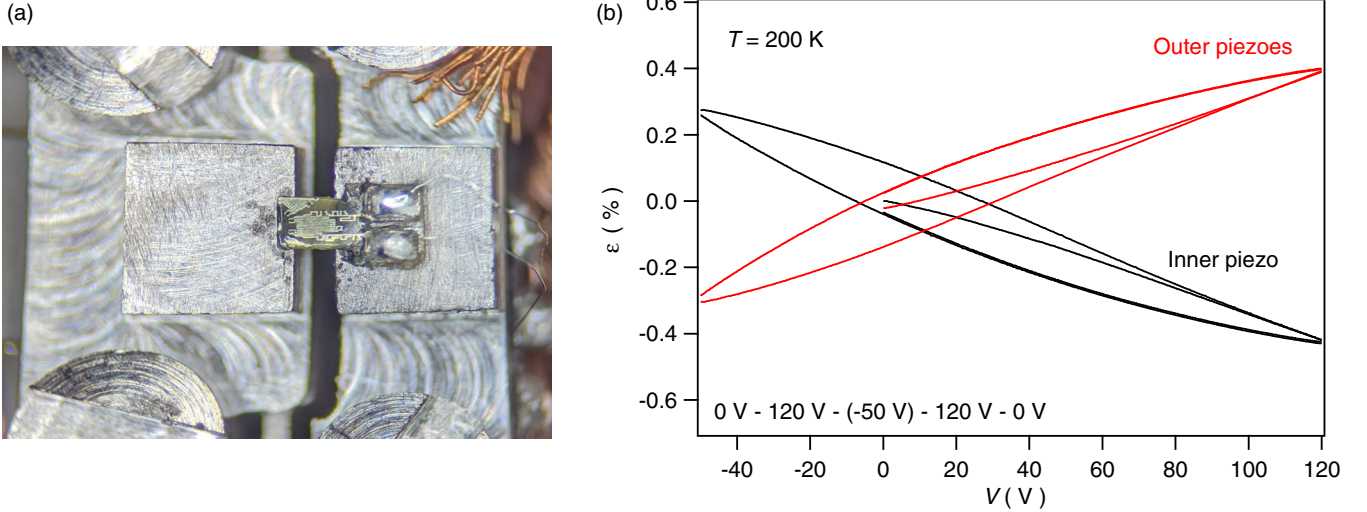


FIG. 7. Strain measurements via strain gauge. (a) A picture of the strain gauge mounted on fixtures. (b) Strain responses as a function of applied voltage on piezo actuators.

coherence-limiting scattering processes that occur during photoemission. While a quantitative explanation for this effect is beyond the scope of this study, we can suggest four qualitative explanations: (1) the screening near the surface is reduced by the absence of metallic topological states in the WTI phase, thus the scattering of bulk states near the surface (that dominate the ARPES signal) is enhanced in the WTI phase. This leads to the QP-like increase in scattering rates towards higher binding energy in the WTI phase; (2) tensile strain reduces the electron density along the Hf chains, thus similarly reducing the bulk screening and enhancing the QP scattering rate in the bulk; (3) defects such as dislocations are created upon tensile strain and reversibly destroyed when strain is relieved or compressive strain applied (We find this explanation unlikely given that we are below the plastic deformation regime, but we mention the possibility for completeness.); (4) electron-phonon effect through varying the Debye temperature with strain or defects. (We find this scenario to be unlikely as

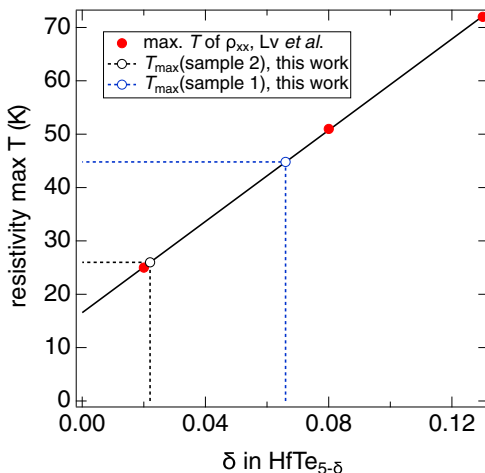


FIG. 8. Uniaxial stress cell for ARPES.

well, as the temperature effect is smaller than what we have measured with strain and defect. Future experiments at low temperatures may provide further clarity on this matter.)

Since we can assume that the diffuse background is dominated by the QP scattering of bulk state [46], the key to distinguishing effects (1) and (2) is the behavior of the momentum broadening of the bulk states with strain. For weakly correlated systems, the bulk states' momentum width  $\Delta k_{\text{bulk}}(\omega)$  at binding energy  $\omega$  from ARPES is directly proportional to the imaginary part of the self-energy function, which reflects the electron lifetime to all scattering from phonons, defects, or other electrons. For (1), we would expect an abrupt general increase in  $\Delta k_{\text{bulk}}(\omega)$  as we transition from STI to WTI, and for (2) we would expect a continual decrease in scattering as we go from tensile to compressive strain, regardless of topological phase transition.

While our analysis of the bulk states' momentum spread  $\Delta k_{\text{bulk}}(\omega)$  has not revealed a clear evolution with strain (see Fig. 15), favoring explanation (1), it remains possible that the changes in  $\Delta k_{\text{bulk}}(\omega)$  are below our experimental resolution, or that the observed  $\Delta k_{\text{bulk}}(\omega)$  is dominated by inhomogeneous broadening effects.

## V. CONCLUSION

In conclusion, we have demonstrated that ARPES spectra change with varying Te vacancies in  $\text{HfTe}_5$ . Surprisingly, these changes were reversed with the application of uniaxial stress. The results strongly suggest that the self-energy of both surface and bulk electronic (trivial) states are strongly impacted by the presence of topological surface states, an effect not seen before in ARPES to our knowledge. Our results further demonstrate strain control of topological states as a new method to tune or optimize the coherence of electronic excitations, even overcoming scattering by unavoidably present defects, to improve the performance of quantum materials in new device schemes.

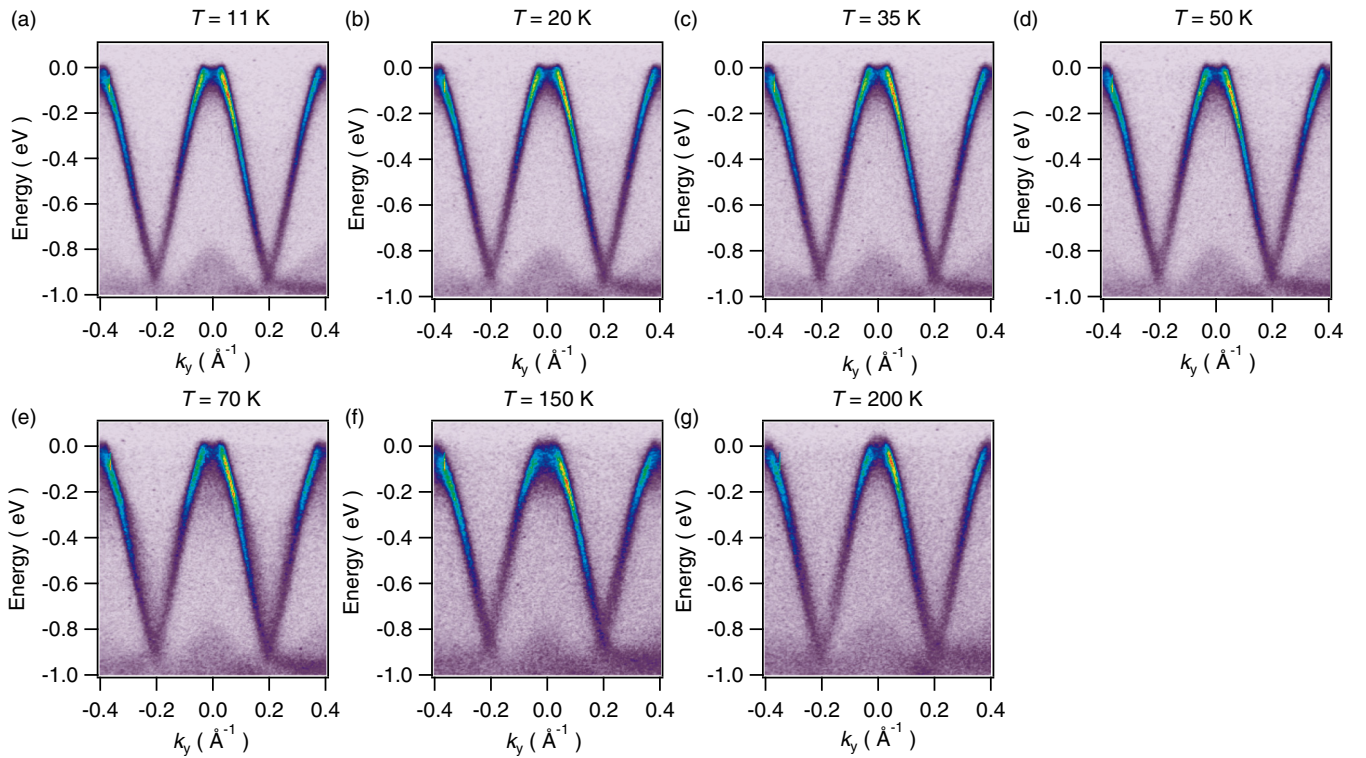


FIG. 9. Temperature-dependent band structures in HfTe<sub>5</sub>. Band dispersion at indicated temperatures between 11 and 200 K.

### ACKNOWLEDGMENTS

The authors thank Lu Li for helpful discussions. This material is based upon work at the QSA, supported by the U.S. Department of Energy, Office of Science, National Quantum Information Science Research Centers. This research used resources of the Advanced Light Source, which is a DOE Office of Science User Facility under Contract No. DE-AC02-05CH11231. This work was also supported by the DOE's Quantum Information Science Enabled Discovery (QuantISED) for High Energy Physics (KA2401032). Computational resources were provided by the National Energy Research Scientific Computing Center and the Molecular

Foundry, DOE Office of Science User Facilities supported under Contract No. DEAC02-05-CH11231. The work performed at the Molecular Foundry was supported by the Office of Science, Office of Basic Energy Sciences, of the U.S. Department of Energy under the same contract. O.A.A. acknowledges helpful discussions with I. Na and E. Banyas.

### APPENDIX

#### 1. Uniaxial stress cell

The uniaxial stress cell we used for this experiment is based on three piezoelectric stacks, similar to Ref. [47]. As

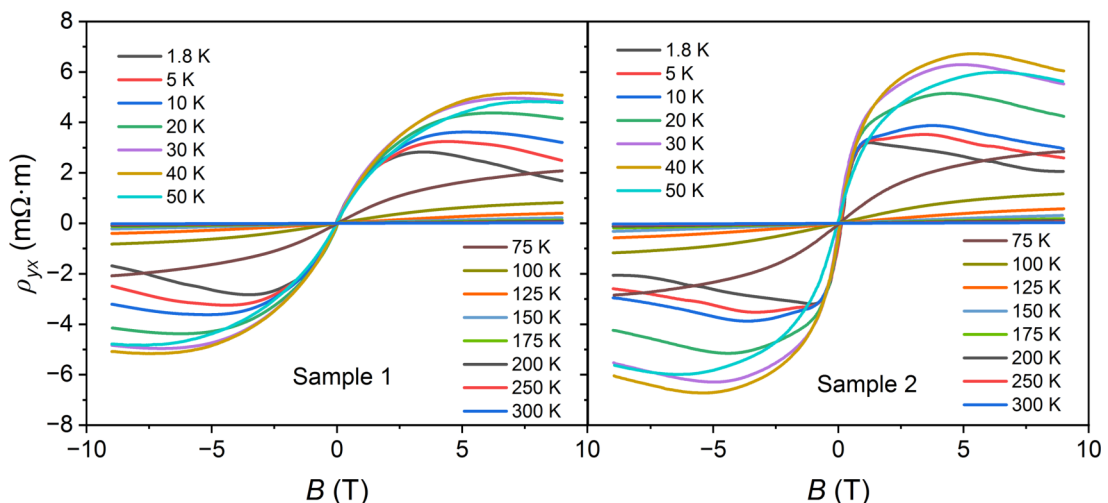


FIG. 10. Temperature-dependent Hall effect on (a) sample 1 with more defect and (b) sample 2 with less defect.

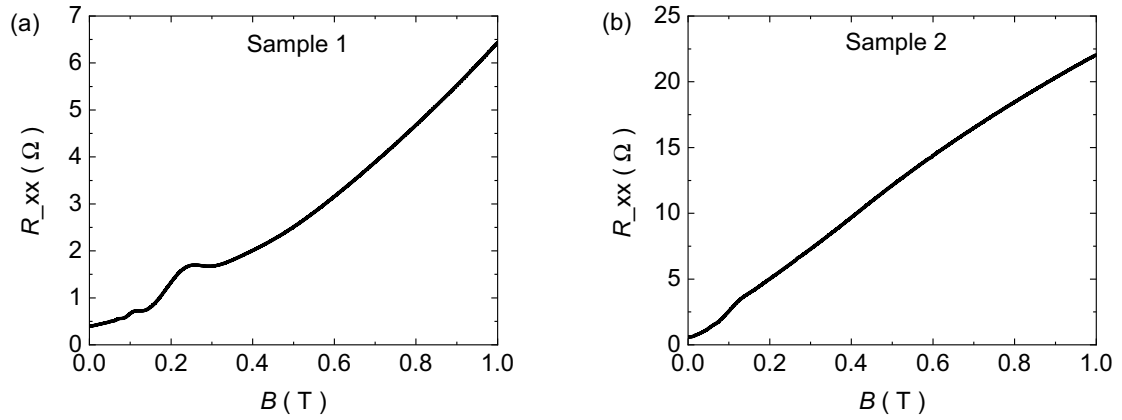


FIG. 11. Quantum oscillation results on sample 1 and 2. (a), (b) Resistivity as a function of the applied magnetic field for sample 1 and 2, respectively.

we have eight available electrical channels on our system, we used four to control the piezoelectric stacks and the rest of the four channels for strain gauge measurements. We attached a Cu thermal braiding near the sample to ground the sample and achieve better temperature control. In addition, we put a Cu shielding on top of the cell to shield the field from the piezoelectric stacks, as shown in Fig. 6 on the right side.

## 2. Strain measurements

The strain was measured using a strain gauge (C5K-XX-S5198-350/39F, Micro-Measurements.) mounted with the Stycast epoxy (2850FT) underneath. We first drive the inner piezo actuator from 0 to 120 V, followed by  $-50$  V, back to 120 V, and ended up at 0 V. While applying voltage on the inner piezo actuator; the outer piezo actuators were connected

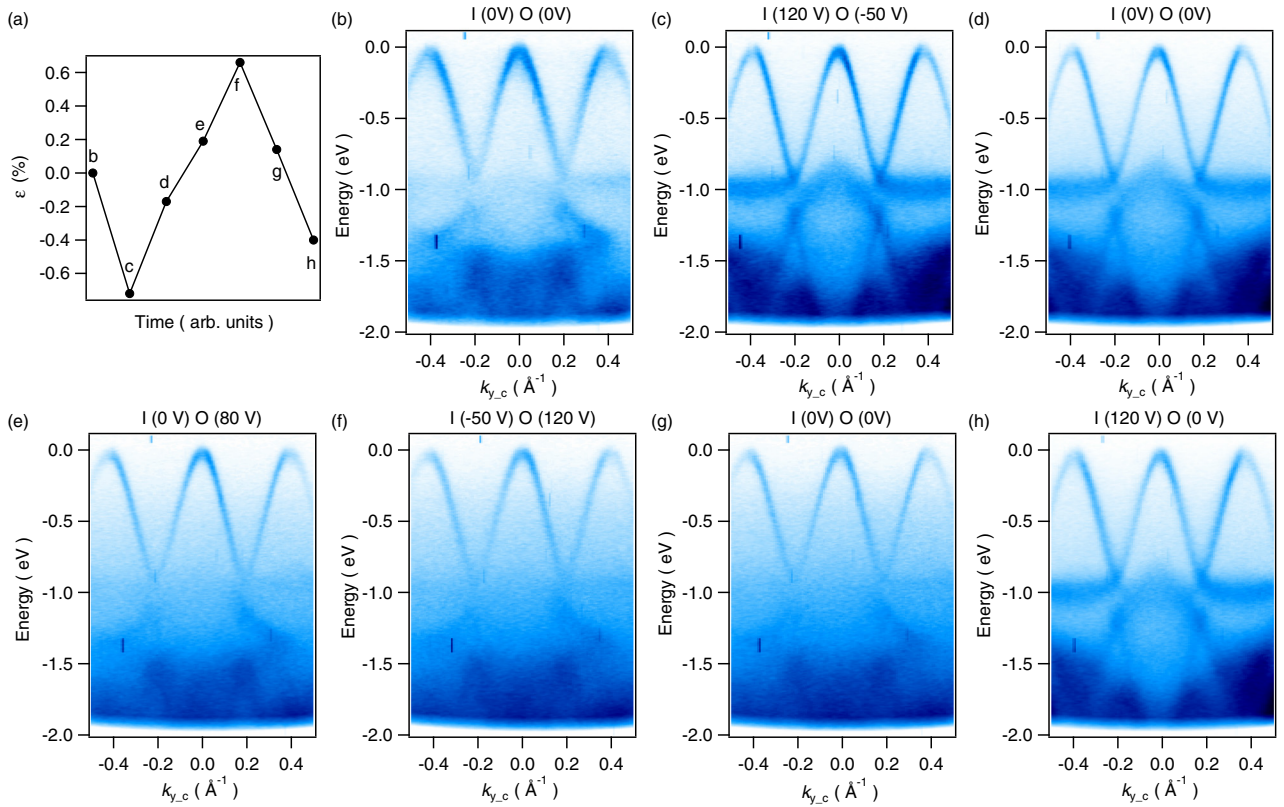


FIG. 12. Strain-dependent band structure. (a) Estimated strain based on strain gauge measurement. Band structure cut along the  $\Gamma$ -Z (crystallographic  $c$ ) direction of  $\text{HfTe}_5$  with the applied voltage: (b) inner piezo actuator of 0 V and outer piezo actuators of 0 V, (c) inner piezo actuator of 120 V and outer piezo actuators of  $-50$  V, (d) inner piezo actuator of 0 V and outer piezo actuators of 0 V, (e) inner piezo actuator of 0 V and outer piezo actuators of 80 V, (f) inner piezo actuator of  $-50$  V and outer piezo actuators of 120 V, (g) inner piezo actuator of 0 V and outer piezo actuators of 0 V, and (h) inner piezo actuator of 120 V and outer piezo actuators of 0 V.

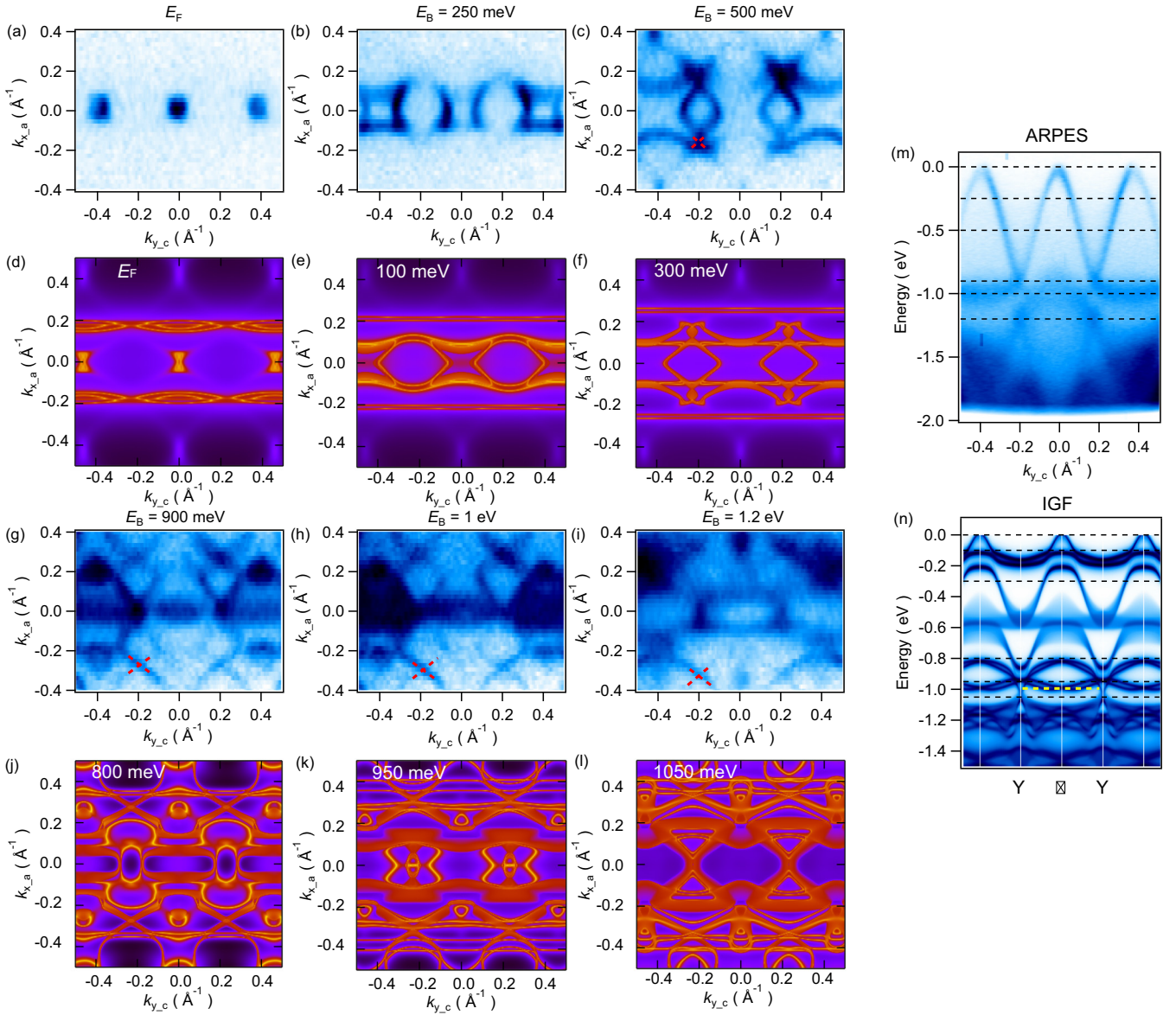


FIG. 13. Constant energy contour plots. (a)–(c) Constant energy contour plots of compressed sample 2 at  $E_F$ ,  $E_B = 250$  meV,  $E_B = 500$  meV, respectively. (d)–(f) Constant energy contour plots from IGF calculations at  $E_F$ ,  $E_B = 100$  meV,  $E_B = 300$  meV, respectively. (g)–(i) Constant energy contour plots of compressed sample 2 at  $E_B = 900$ ,  $E_B = 1$  eV,  $E_B = 1.2$  eV, respectively. (j)–(l) Constant energy contour plots from IGF calculations at  $E_B = 800$  meV,  $E_B = 950$  meV,  $E_B = 1.05$  eV, respectively. (m) Band structure of compressed sample 2 along the  $k_y$ . The dashed line marks the energy from which the constant energy contour plots are taken. (n) Band structure from IGF calculations along the  $k_y$ . The dashed line marks the energy from which the constant energy contour plots are taken. Red dashed lines indicate another linear band crossing point.

in a short circuit. At the same time, we measured changes in the resistance of the strain gauge. With the given gauge factor of 1.84 from the manufacturer, the strain was calculated. The results are shown in Fig. 7(b) in the black line. A clear hysteresis was detected with the maximum compressive strain of  $\sim -0.42\%$  at 120 V and maximum tensile strain of  $\sim 0.27\%$  at  $-50$  V. We then put the inner piezo actuator in a short circuit and derive the outer piezo actuators with the same applied voltage sequence. The red line in Fig. 7(b) shows a similar hysteresis loop but the opposite sign compared to the hysteresis loop from the inner piezo actuator. The maximum compressive strain of  $\sim -0.3\%$  at  $-50$  V and the maximum tensile strain of  $\sim -0.39\%$  at 120 V were observed.

### 3. Estimate of defect density

For the Te-poor compound  $\text{HfTe}_{5-\delta}$ , Lv *et al.* [25] have reported a linear relationship between the Te deficit  $\delta$  with the temperature of the maximum longitudinal resistivity  $\rho_{xx}$ , which is plotted in Fig. 8 (red dots). Since this temperature is very similar to  $T_{\text{max}}$  as defined in our main text, we have used their transport measurements to derive estimates of  $\delta$  for our samples (1, 2), which are  $\delta = (0.066, 0.022)$ , respectively.

The samples were also measured with a JEOL JSM-7800F scanning electron microscope, operated in low-vacuum mode with dry  $\text{N}_2$  used as the charge neutralizing gas, using an Oxford XMaxN 80mm<sup>2</sup> energy dispersive x-ray spectroscopy

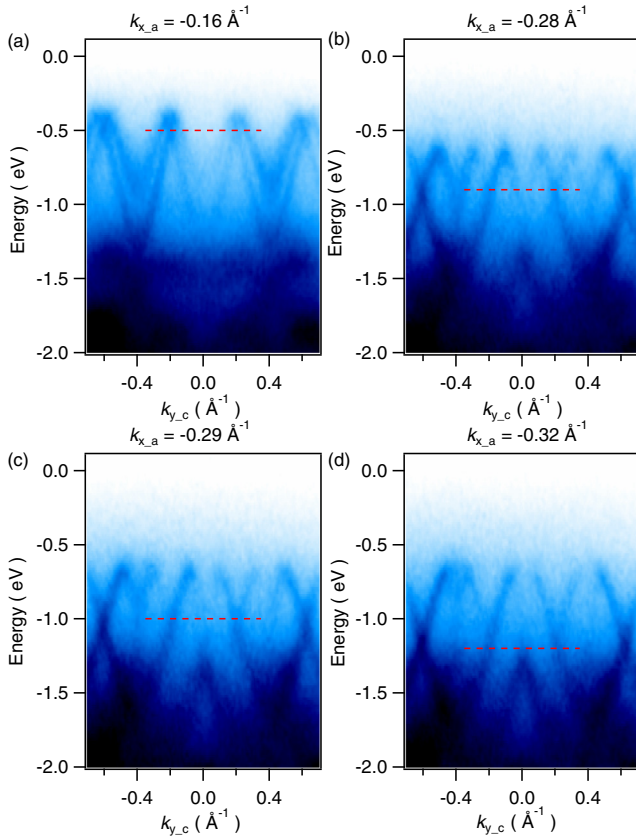


FIG. 14. Electronic band dispersion in compressed HfTe<sub>5</sub> at the crossing points (a)–(d) Electronic band dispersion at  $k_x = -0.16 \text{ \AA}^{-1}$ ,  $k_x = -0.28 \text{ \AA}^{-1}$ ,  $k_x = -0.29 \text{ \AA}^{-1}$ , and  $k_x = -0.32 \text{ \AA}^{-1}$  that are marked in Figs. 13(c)–13(f), respectively. Red dashed lines indicate the Dirac point at  $E_B = 500 \text{ meV}$ ,  $900 \text{ meV}$ ,  $1 \text{ eV}$ , and  $1.2 \text{ eV}$ .

(EDS) detector and Oxford AZTec v.3.3 software for EDS measurements. Measurements were made using an accelerating potential of 20 kV. The measurements were carried out multiple points in each samples. The averaged values for Sample 1 and Sample 2 are HfTe<sub>4.18</sub> and HfTe<sub>4.58</sub>, respectively. It is crucial to consider that standardless EDS data is semi-quantitative, and absolute values should be interpreted with caution. However, the comparison between the two samples is clear: Sample 1 exhibits more Te vacancy than Sample 2.

#### 4. Temperature evolution of the band structures in HfTe<sub>5</sub>

Figure 9 shows temperature-dependent band structures of sample 1 measured along  $\Gamma$ -Y direction. The plot clearly demonstrates that the hole band progressively moves down in energy as the temperature rises. At around 200 K, the top of the hole band almost reaches the chemical potential. The chemical potential at low temperature aligns with that of sample 2 and a previous study in Ref. [18] but differs from Ref. [48].

This discrepancy may be attributed to different sample defects or different measurement conditions. Reference [25] indicates that HfTe<sub>4.98</sub> and HfTe<sub>4.87</sub> have dominant electron carriers at low temperatures, whereas HfTe<sub>4.92</sub> displays hole carriers. Our samples, as depicted in Fig. 8, fall between

HfTe<sub>4.98</sub> and HfTe<sub>4.87</sub>, indicating hole-dominant carriers at low temperatures, consistent with our temperature-dependent ARPES results. This scenario can also account for the low-temperature band structure discrepancies in Refs. [18,48]. In addition, our Hall effect experiments consistently show hole carriers as the dominant type throughout the measured temperature range. These results are in line with theoretical insights as seen in Ref. [49], where the chemical potential remains unchanged with temperature variations for hole-doped samples.

Another possible source of differences could be attributed to the choice of light source. Both our paper and Ref. [18] used light sources with higher photon energy and true high-symmetry points, whereas the paper in Ref. [48] employed a laser source with an energy of 6.994 eV. This resulted in slight variations in measurement depths and a potential misalignment of the laser source with a high-symmetry point.

#### 5. Hall effect

We conducted Hall effect measurements on both samples across various temperatures, as illustrated in Fig. 10. The results reveal a pronounced nonmonotonic behavior in Hall resistivity as a function of the applied magnetic field. Interpreting this nonlinearity, there are multiple potential factors at play, including the existence of multiple bands within the system and the influence of anomalous Hall effect (AHE). While it's essential to acknowledge the AHE, particularly concerning its connection to Berry curvature, the prevailing approach in the field has been to employ a two-band model to fit the data. Our fitting analysis using a two-band model indicates that the dominant carrier is the hole carrier, with sample 1 exhibiting a slightly higher carrier density than sample 2. Future studies involving a thorough analysis of the Hall effect, considering both the multiband model and anomalous Hall effect (AHE), will be necessary to determine carrier density details.

#### 6. Quantum oscillation

The quantum oscillation results shown in Fig. 11 also suggest that sample 1 possesses a larger pocket than sample 2, which also matches with Hall effect analysis. An additional intriguing observation is that sample 1, despite having a higher level of defects, exhibits more distinct quantum oscillation results. This observation provides further support for our hypothesis of a screening effect arising from the topological surface state.

#### 7. Strain-dependent band structure

Figure 12 presents band structure changes with full-cycle piezo actuator movements (0 V-compress-tensile-compress). It demonstrates not only apparent changes in band structure with the applied uniaxial stress but also reproducible results.

From these data points, we identify a phase transition occurring within the range of 0-0.2% compressive stress, based on the band structure changes approximately 1 eV below the Fermi energy. Considering the DFT level happens at  $\sim 1.6\%$  tensile strain ( $a_c \sim 4.016 \text{ \AA}$ ), then the relative error in the critical lattice constant is  $\sim 1.26\%$ , or an absolute error of

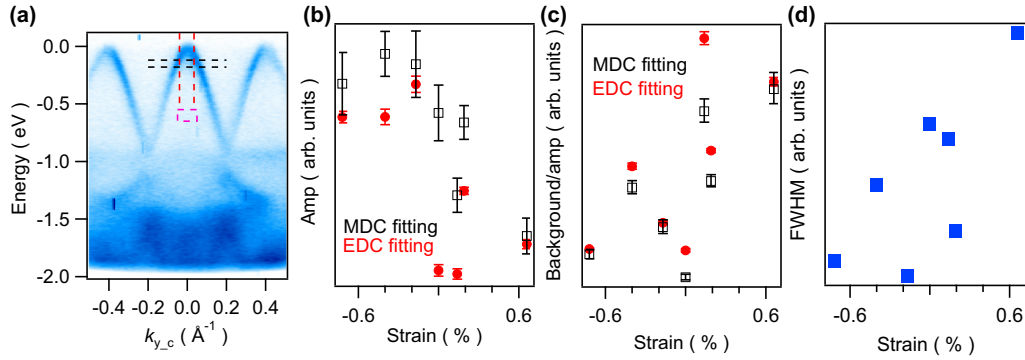


FIG. 15. Detailed analysis of ARPES data. (a) Band structure of unstrained sample 2 along the  $\Gamma$ -Y direction. Black dashed lines mark the binning range for the momentum distribution curve (MDC) fitting. Red dashed lines indicate the binning range for the energy distribution curve (EDC) fitting. The magenta rectangular box shows the area where the averaged background is obtained. (b) Average amplitudes of bands based on the MDC and EDC fitting in the marked range shown in panel (a). (c) Normalized background signal over amplitudes of bands. The amplitudes are based on panel (b). (d) Full width half maximum (FWHM) of MDC peak at 0.27 eV below the Fermi energy.

$\sim 0.05$   $\text{\AA}$ . A 5 pm error is quite reasonable at the DFT level, and a 1.26% relative error is well within the error margin for the exchange-correlation functional we used.

### 8. Comparison between ARPES and IGF calculations

Figures 13(a)–13(c) and 13(g)–13(i) show constant energy contour plots of  $\text{HfTe}_5$  under compressive strain (sample 2). Corresponding IGF calculations are also plotted in Figs. 13(d)–13(f) and 13(j)–13(l). The binding energies of each plot, Figs. 13(a)–13(l), are marked in Figs. 13(m) and 13(n). Comparing ARPES and IGF calculations, we find that sample 2 with compressive strain (or unstrained sample 1) is very close to but not exactly the same as the equilibrium IGF calculation results. First of all, the chemical potential is shifted about 150 meV downward in ARPES data compared to the IGF calculations. More specifically, the Fermi surface from ARPES measurement is composed of dots which are the residual intensities from the top of the hole bands below  $E_F$  [Fig. 13(a)]. However,  $E_F$  crosses the hole bands in the IGF calculation. As a result, the astroid shape of the Fermi surface is observed in the IGF calculations [Fig. 13(d)]. The astroids become more clear at higher binding energies in both ARPES and IGF calculation results [Figs. 13(b), 13(c), and 13(d)–13(f)]. ARPES results at the binding energies of 250 and 500 meV are very similar to the IGF calculation results at 100 and 300 meV, respectively. This means 150–

200 meV band shifts in ARPES data. Second, the spacing between two surface bands,  $\alpha$ , and  $\beta$ , gets larger with tensile strain in the IGF calculations [see Figs. 5(d)–5(f)]. In fact, the spacing between the surface bands in compressed sample 2 and unstrained sample 1 is slightly larger than that of the IGF calculation at equilibrium, which means the samples at those conditions are slightly stretched.

### 9. Linear band crossings away from high symmetry points

The astroids shown in Fig. 13 start to cross at  $E_B = 500$  meV. Crossing points are marked with red dashed lines in Figs. 13(c) and 13(g)–13(i). With larger binding energy, the points move outwards in the  $k_x$  direction. Interestingly, the crossing points of the steroids marked in Fig. 13 with red dashed lines correspond to linear crossing in the band structure as shown in Fig. 14.

### 10. Effect of strain on the topological phase of gap (I)

Table II shows the topological invariants and classification of gap (I) in  $\text{HfTe}_5$  at different levels of strain. The topological phase transition between the STI and WTI phases happens between 1.5% and 1.75% tensile strain. See the methods section for details of the calculation.

We note that the DFT calculations underestimate  $a$  by 0.43% compared to the value of  $a = 3.97$   $\text{\AA}$  measured in our samples (see Methods). However, since DFT is a zero-kelvin, ground state theory, our calculations do not account for finite-temperature effects such as lattice expansion, and our  $a$  lattice constant is within 0.27% of the measured value at 10 K ( $a = 3.964$   $\text{\AA}$ ) [37]. Since DFT typically has errors of 1%–2% in the lattice constant [50,51], a direct comparison of the strain values with experiment is not well motivated. However, by selecting a range of strains, we can observe the trends in behaviors, and suggest the evolution of the phase diagram with strain, even if the exact value does not coincide with that measured in experiment.

TABLE III. Bond lengths in  $\text{\AA}$  as shown in Fig. 2(a), for structures with different Te vacancies and strain.

Structure	A	B	C
2% Compressive	3.876	7.547	7.337
Equilibrium	3.953	7.545	7.327
2% Tensile	4.034	7.554	7.311
Te-1 Vacancy	3.927	7.555	7.299
Te-2 Vacancy	3.956	7.568	7.322
Te-3 Vacancy	3.958	7.561	7.302

### 11. Effect of vacancies and strain on bond lengths

The structural changes are quantified by comparing the Hf-Hf nearest-neighbor distances in the A, B, and C directions as indicated on the crystal structure in Fig. 2(a) with the values for the stoichiometric case. For each calculation, one Te vacancy was included in a  $2 \times 2 \times 2$  super cell comprising 16 formula units of HfTe<sub>5</sub> resulting in a 1.25% defect density. The results are tabulated in Table III and plotted in Fig. 2(d).

### 12. Detailed analysis of ARPES data at different strains

Figures 15(b) and 15(c) indicate a decrease in the amplitude of the bands and an increase of background noise with tensile strain in HfTe<sub>5</sub>. Additionally, in Fig. 15(d), the linewidth of peaks broadens with the application of tensile stress. However, it is not clear whether a sharp transition occurs within the 0–0.2% compressive strain range, as the data are somewhat scattered.

- [1] Y. Chen, J.-H. Chu, J. Analytis, Z. Liu, K. Igarashi, H.-H. Kuo, X. Qi, S.-K. Mo, R. Moore, D. Lu *et al.*, Massive Dirac fermion on the surface of a magnetically doped topological insulator, *Science* **329**, 659 (2010).
- [2] D. Zhang, M. Shi, T. Zhu, D. Xing, H. Zhang, and J. Wang, Topological axion states in the magnetic insulator MnBi<sub>2</sub>Te<sub>4</sub> with the quantized magnetoelectric effect, *Phys. Rev. Lett.* **122**, 206401 (2019).
- [3] J. Li, Y. Li, S. Du, Z. Wang, B.-L. Gu, S.-C. Zhang, K. He, W. Duan, and Y. Xu, Intrinsic magnetic topological insulators in van der Waals layered MnBi<sub>2</sub>Te<sub>4</sub>-family materials, *Sci. Adv.* **5**, eaaw5685 (2019).
- [4] M. M. Otrokov, I. I. Klimovskikh, H. Bentmann, D. Estyunin, A. Zeugner, Z. S. Aliev, S. Gaß, A. Wolter, A. Koroleva, A. M. Shikin *et al.*, Prediction and observation of an antiferromagnetic topological insulator, *Nature (London)* **576**, 416 (2019).
- [5] N. H. Jo, L.-L. Wang, R.-J. Slager, J. Yan, Y. Wu, K. Lee, B. Schränk, A. Vishwanath, and A. Kaminski, Intrinsic axion insulating behavior in antiferromagnetic MnBi<sub>6</sub>Te<sub>10</sub>, *Phys. Rev. B* **102**, 045130 (2020).
- [6] N. C. Frey, M. K. Horton, J. M. Munro, S. M. Griffin, K. A. Persson, and V. B. Shenoy, High-throughput search for magnetic and topological order in transition metal oxides, *Sci. Adv.* **6**, eabd1076 (2020).
- [7] Q. Li, D. E. Kharzeev, C. Zhang, Y. Huang, I. Pletikosić, A. Fedorov, R. Zhong, J. Schneeloch, G. Gu, and T. Valla, Chiral magnetic effect in ZrTe<sub>5</sub>, *Nat. Phys.* **12**, 550 (2016).
- [8] R. Y. Chen, Z. G. Chen, X.-Y. Song, J. A. Schneeloch, G. D. Gu, F. Wang, and N. L. Wang, Magnetoinfrared spectroscopy of Landau levels and Zeeman splitting of three-dimensional massless Dirac fermions in ZrTe<sub>5</sub>, *Phys. Rev. Lett.* **115**, 176404 (2015).
- [9] R. Y. Chen, S. J. Zhang, J. A. Schneeloch, C. Zhang, Q. Li, G. D. Gu, and N. L. Wang, Optical spectroscopy study of the three-dimensional Dirac semimetal ZrTe<sub>5</sub>, *Phys. Rev. B* **92**, 075107 (2015).
- [10] G. Zheng, J. Lu, X. Zhu, W. Ning, Y. Han, H. Zhang, J. Zhang, C. Xi, J. Yang, H. Du, K. Yang, Y. Zhang, and M. Tian, Transport evidence for the three-dimensional Dirac semimetal phase in ZrTe<sub>5</sub>, *Phys. Rev. B* **93**, 115414 (2016).
- [11] L. Shen, M. Wang, S. Sun, J. Jiang, X. Xu, T. Zhang, Q. Zhang, Y. Lv, S. Yao, Y. Chen, M. Lu, Y. Chen, C. Felser, B. Yan, Z. Liu, L. Yang, and Y. Chen, Spectroscopic evidence for the gapless electronic structure in bulk ZrTe<sub>5</sub>, *J. Electron Spectrosc. Relat. Phenom.* **219**, 45 (2017).
- [12] R. Wu, J.-Z. Ma, S.-M. Nie, L.-X. Zhao, X. Huang, J.-X. Yin, B.-B. Fu, P. Richard, G.-F. Chen, Z. Fang, X. Dai, H.-M. Weng, T. Qian, H. Ding, and S. H. Pan, Evidence for topological edge states in a large energy gap near the step edges on the surface of ZrTe<sub>5</sub>, *Phys. Rev. X* **6**, 021017 (2016).
- [13] X.-B. Li, W.-K. Huang, Y.-Y. Lv, K.-W. Zhang, C.-L. Yang, B.-B. Zhang, Y. B. Chen, S.-H. Yao, J. Zhou, M.-H. Lu, L. Sheng, S.-C. Li, J.-F. Jia, Q.-K. Xue, Y.-F. Chen, and D.-Y. Xing, Experimental observation of topological edge states at the surface step edge of the topological insulator ZrTe<sub>5</sub>, *Phys. Rev. Lett.* **116**, 176803 (2016).
- [14] G. Manzoni, A. Sterzi, A. Crepaldi, M. Diego, F. Cilento, M. Zacchigna, P. Bugnon, H. Berger, A. Magrez, M. Grioni, and F. Parmigiani, Ultrafast optical control of the electronic properties of ZrTe<sub>5</sub>, *Phys. Rev. Lett.* **115**, 207402 (2015).
- [15] Y. Zhang, C. Wang, L. Yu, G. Liu, A. Liang, J. Huang, S. Nie, X. Sun, Y. Zhang, B. Shen *et al.*, Electronic evidence of temperature-induced Lifshitz transition and topological nature in ZrTe<sub>5</sub>, *Nat. Commun.* **8**, 15512 (2017).
- [16] L. Moreschini, J. C. Johannsen, H. Berger, J. Denlinger, C. Jozwiak, E. Rotenberg, K. S. Kim, A. Bostwick, and M. Grioni, Nature and topology of the low-energy states in ZrTe<sub>5</sub>, *Phys. Rev. B* **94**, 081101(R) (2016).
- [17] G. Manzoni, L. Gragnaniello, G. Autès, T. Kuhn, A. Sterzi, F. Cilento, M. Zacchigna, V. Enenkel, I. Vobornik, L. Barba, F. Bisti, P. Bugnon, A. Magrez, V. N. Strocov, H. Berger, O. V. Yazyev, M. Fonin, F. Parmigiani, and A. Crepaldi, Evidence for a strong topological insulator phase in ZrTe<sub>5</sub>, *Phys. Rev. Lett.* **117**, 237601 (2016).
- [18] S. Liu, M. Wang, C. Chen, X. Xu, J. Jiang, L. Yang, H. Yang, Y. Lv, J. Zhou, Y. Chen *et al.*, Experimental observation of conductive edge states in weak topological insulator candidate HfTe<sub>5</sub>, *APL Mater.* **6**, 121111 (2018).
- [19] N. L. Nair, P. T. Dumitrescu, S. Channa, S. M. Griffin, J. B. Neaton, A. C. Potter, and J. G. Analytis, Thermodynamic signature of Dirac electrons across a possible topological transition in ZrTe<sub>5</sub>, *Phys. Rev. B* **97**, 041111(R) (2018).
- [20] D. N. McIlroy, S. Moore, D. Zhang, J. Wharton, B. Kempton, R. Littleton, M. Wilson, T. M. Tritt, and C. G. Olson, Observation of a semimetal-semiconductor phase transition in the intermetallic ZrTe<sub>5</sub>, *J. Phys.: Condens. Matter* **16**, L359 (2004).
- [21] F. Tang, Y. Ren, P. Wang, R. Zhong, J. Schneeloch, S. A. Yang, K. Yang, P. A. Lee, G. Gu, Z. Qiao *et al.*, Three-dimensional quantum Hall effect and metal-insulator transition in ZrTe<sub>5</sub>, *Nature (London)* **569**, 537 (2019).
- [22] Y. Liu, X. Yuan, C. Zhang, Z. Jin, A. Narayan, C. Luo, Z. Chen, L. Yang, J. Zou, X. Wu *et al.*, Zeeman splitting and dynamical

- mass generation in Dirac semimetal ZrTe<sub>5</sub>, *Nat. Commun.* **7**, 12516 (2016).
- [23] S. Galeski, T. Ehmcke, R. Wawrzyńczak, P. M. Lozano, K. Cho, A. Sharma, S. Das, F. Küster, P. Sessi, M. Brando *et al.*, Origin of the quasi-quantized Hall effect in ZrTe<sub>5</sub>, *Nat. Commun.* **12**, 3197 (2021).
- [24] P. Shahi, D. J. Singh, J. P. Sun, L. X. Zhao, G. F. Chen, Y. Y. Lv, J. Li, J.-Q. Yan, D. G. Mandrus, and J.-G. Cheng, Bipolar conduction as the possible origin of the electronic transition in pentatellurides: Metallic vs semiconducting behavior, *Phys. Rev. X* **8**, 021055 (2018).
- [25] Y.-Y. Lv, X. Li, L. Cao, D. Lin, S.-H. Yao, S.-S. Chen, S.-T. Dong, J. Zhou, Y. B. Chen, and Y.-F. Chen, Tunable resistance or magnetoresistance cusp and extremely large magnetoresistance in defect-engineered HfTe<sub>5-δ</sub> single crystals, *Phys. Rev. Appl.* **9**, 054049 (2018).
- [26] Y. Zhou, J. Wu, W. Ning, N. Li, Y. Du, X. Chen, R. Zhang, Z. Chi, X. Wang, X. Zhu, P. Lu, C. Ji, X. Wan, Z. Yang, J. Sun, W. Yang, M. Tian, Y. Zhang, and H. Kwang Mao, Pressure-induced superconductivity in a three-dimensional topological material ZrTe<sub>5</sub>, *Proc. Natl. Acad. Sci. USA* **113**, 2904 (2016).
- [27] J. Mutch, W.-C. Chen, P. Went, T. Qian, I. Z. Wilson, A. Andreev, C.-C. Chen, and J.-H. Chu, Evidence for a strain-tuned topological phase transition in ZrTe<sub>5</sub>, *Sci. Adv.* **5**, eaav9771 (2019).
- [28] P. Zhang, R. Noguchi, K. Kuroda, C. Lin, K. Kawaguchi, K. Yaji, A. Harasawa, M. Lippmaa, S. Nie, H. Weng *et al.*, Observation and control of the weak topological insulator state in ZrTe<sub>5</sub>, *Nat. Commun.* **12**, 406 (2021).
- [29] Y. Hochberg, Y. Kahn, M. Lisanti, K. M. Zurek, A. G. Grushin, R. Ilan, S. M. Griffin, Z.-F. Liu, S. F. Weber, and J. B. Neaton, Detection of sub-meV dark matter with three-dimensional Dirac materials, *Phys. Rev. D* **97**, 015004 (2018).
- [30] B. Monserrat and A. Narayan, Unraveling the topology of ZrTe<sub>5</sub> by changing temperature, *Phys. Rev. Res.* **1**, 033181 (2019).
- [31] N. H. Jo, L.-L. Wang, P. P. Orth, S. L. Bud'ko, and P. C. Canfield, Magnetoelastoresistance in WTe<sub>2</sub>: Exploring electronic structure and extremely large magnetoresistance under strain, *Proc. Natl. Acad. Sci. USA* **116**, 25524 (2019).
- [32] G. Kresse and J. Hafner, *Ab initio* molecular dynamics for liquid metals, *Phys. Rev. B* **47**, 558 (1993).
- [33] G. Kresse and J. Hafner, *Ab initio* molecular-dynamics simulation of the liquid-metal–amorphous-semiconductor transition in germanium, *Phys. Rev. B* **49**, 14251 (1994).
- [34] G. Kresse and J. Furthmüller, Efficiency of *ab initio* total energy calculations for metals and semiconductors using a plane-wave basis set, *Comput. Mater. Sci.* **6**, 15 (1996).
- [35] G. Kresse and J. Furthmüller, Efficient iterative schemes for *ab initio* total-energy calculations using a plane-wave basis set, *Phys. Rev. B* **54**, 11169 (1996).
- [36] G. Kresse and D. Joubert, From ultrasoft pseudopotentials to the projector augmented-wave method, *Phys. Rev. B* **59**, 1758 (1999).
- [37] H. Fjellvåg and A. Kjekshus, Structural properties of ZrTe<sub>5</sub> and HfTe<sub>5</sub> as seen by powder diffraction, *Solid State Commun.* **60**, 91 (1986).
- [38] G. Pizzi, V. Vitale, R. Arita, S. Blügel, F. Freimuth, G. Géranton, M. Gibertini, D. Gresch, C. Johnson, T. Koretsune, J. Ibañez-Azpiroz, H. Lee, J. Li, D. Marchand, A. Marrazzo, Y. Mokrousov, J. Mustafa, Y. Nohara, Y. Nomura, L. Paulatto *et al.*, Wannier90 as a community code: New features and applications, *J. Phys.: Condens. Matter* **32**, 165902 (2020).
- [39] Q. Wu, S. Zhang, H.-F. Song, M. Troyer, and A. A. Soluyanov, Wanniertools: An open-source software package for novel topological materials, *Comput. Phys. Commun.* **224**, 405 (2018).
- [40] Y. He, Y. Jiang, T. Zhang, H. Huang, C. Fang, and Z. Jin, Sympto: An automatic tool for calculating topological properties of nonmagnetic crystalline materials, *Chin. Phys. B* **28**, 087102 (2019).
- [41] M. Iraola, J. L. Mañes, B. Bradlyn, M. K. Horton, T. Neupert, M. G. Vergniory, and S. S. Tsirkin, Irrep: Symmetry eigenvalues and irreducible representations of *ab initio* band structures, *Comput. Phys. Commun.* **272**, 108226 (2022).
- [42] L. Elcoro, B. Bradlyn, Z. Wang, M. G. Vergniory, J. Cano, C. Felser, B. A. Bernevig, D. Orobengoa, G. de la Flor, and M. I. Aroyo, Double crystallographic groups and their representations on the Bilbao Crystallographic Server, *J. Appl. Crystallogr.* **50**, 1457 (2017).
- [43] M. G. Vergniory, B. J. Wieder, L. Elcoro, S. S. P. Parkin, C. Felser, B. A. Bernevig, and N. Regnault, All topological bands of all nonmagnetic stoichiometric materials, *Science* **376**, ea9094 (2022).
- [44] L. Fu and C. L. Kane, Topological insulators with inversion symmetry, *Phys. Rev. B* **76**, 045302 (2007).
- [45] L. Fu, C. L. Kane, and E. J. Mele, Topological insulators in three dimensions, *Phys. Rev. Lett.* **98**, 106803 (2007).
- [46] S. Cai, J. Guo, V. A. Sidorov, Y. Zhou, H. Wang, G. Lin, X. Li, Y. Li, K. Yang, A. Li, Q. Wu, J. Hu, S. K. Kushwaha, R. J. Cava, and L. Sun, Independence of topological surface state and bulk conductance in three-dimensional topological insulators, *npj Quantum Mater.* **3**, 62 (2018).
- [47] C. W. Hicks, M. E. Barber, S. D. Ekins, D. O. Brodsky, and A. P. Mackenzie, Piezoelectric-based apparatus for strain tuning, *Rev. Sci. Instrum.* **85**, 065003 (2014).
- [48] Y. Zhang, C. Wang, G. Liu, A. Liang, L. Zhao, J. Huang, Q. Gao, B. Shen, J. Liu, C. Hu, W. Zhao, G. Chen, X. Jia, L. Yu, L. Zhao, S. He, F. Zhang, S. Zhang, F. Yang, Z. Wang *et al.*, Temperature-induced Lifshitz transition in topological insulator candidate HfTe<sub>5</sub>, *Sci. Bull.* **62**, 950 (2017).
- [49] C. Wang, Thermodynamically induced transport anomaly in dilute metals ZrTe<sub>5</sub> and HfTe<sub>5</sub>, *Phys. Rev. Lett.* **126**, 126601 (2021).
- [50] F. Tran, J. Stelzl, and P. Blaha, Rungs 1 to 4 of DFT Jacob's ladder: Extensive test on the lattice constant, bulk modulus, and cohesive energy of solids, *J. Chem. Phys.* **144**, 204120 (2016).
- [51] G.-X. Zhang, A. M. Reilly, A. Tkatchenko, and M. Scheffler, Performance of various density-functional approximations for cohesive properties of 64 bulk solids, *New J. Phys.* **20**, 063020 (2018).